J. Fluid Mech. (2003), *vol.* 486, *pp.* 189–211. © 2003 Cambridge University Press
DOI: 10.1017/S0022112003004567 Printed in the United Kingdom

On the wake structure behind a heated horizontal cylinder in cross-flow

By RENE N. KIEFT[1], C. C. M. RINDT[1]†,
A. A. VAN STEENHOVEN[1] AND G. J. F. VAN HEIJST[2]

[1]Department of Mechanical Engineering, Eindhoven University of Technology, PO Box 513, Eindhoven 5600 MB, The Netherlands

[2]Department of Physics, Eindhoven University of Technology, PO Box 513, Eindhoven 5600 MB, The Netherlands

(Received 21 March 2002 and in revised form 19 November 2002)

This paper describes a numerical and experimental study of the effect of heat input on the behaviour of the vortices shed from a horizontal cylinder in a horizontal cross-flow. The Reynolds number (Re_D) is fixed at 75, while the Richardson number (Ri_D) is varied between 0 and 1 (corresponding to forced and mixed convection, respectively). In this parameter regime the wake consists of a double row of alternately shed vortices. A rather unexpected effect of the induced heat is the downward motion of the shed vortex structures. Detailed experiments and numerical simulations show that this effect is caused by the difference in strength between the two vortex rows. An analysis of the vorticity sources present during the formation process shows that the thermally induced baroclinic vorticity production is mainly responsible for this.

1. Introduction

The mechanism of vortex shedding behind bluff bodies has been attracting the attention of fluid dynamicists for a long time. Recently, there has been a renewed interest into the wake stability. The ever-growing computer resources and the sophisticated experimental techniques available can now be used to acquire a better understanding of the details of the transition process and the route to turbulence for wake flows. Behind an obstacle one commonly observes the formation of more or less coherent structures, and under certain conditions these structures may be shed and advected downstream. The shed structures are primarily responsible for the global wake characteristics such as, for example, the typical shedding frequencies and mixing properties. In the case of a flow around a circular cylinder, the wake takes on the appearance of the celebrated von Kármán vortex street, when the value of the Reynolds number Re_D (based on the cylinder's diameter) is in the range $45 < Re_D < 180$.

Several investigations have been carried out to determine the effects of external sources on the vortex shedding process and the associated wake properties. One such a source is an externally imposed vibration of the cylinder. If the amplitude of the vibration is sufficiently large and its frequency approaches the natural vortex shedding frequency, vortex shedding takes place at this external frequency (Karniadakis & Triantafyllou 1989). Even more interesting is the effect of vibrations on the vortex

---

† Author to whom correspondence should be addressed: c.c.m.rindt@tue.nl

and wake characteristics. For large vibration amplitudes it appears that the staggered pattern formed by the shed vortices entirely disintegrates (Koopmann 1967; Davies 1976; Griffin & Ramberg 1976). Depending on the external frequency and amplitude this can eventually lead to a collapse of the vortex structures within the wake (Griffin & Votaw 1971). The vibrations also influence near-wake characteristics such as the formation length and the shedding mechanism. Although in the previous investigations only radial vibrations were considered, more recent publications have revealed that an oscillating rotation of the cylinder also results in a distortion of the vortex street (Dennis, Nguyen & Kocabiyik 2000).

The vortex distribution in the wake turns out to have a major influence on the wake stability. By using a discrete-vortex approach Karasudani & Funakoshi (1994) investigated the effect of the relative distance between the vortices on the wake and structure stability. They found that for small distances between the vortices within the vortex row, each of the vortex rows transforms into a vortex sheet. In other words, the separate vortex structures merge and the vortex street collapses. This study also showed that the vorticity distribution within the vortex structures has a large influence on this process.

Another way to disturb the vortex shedding process is by heating the cylinder surface. Besides the scientific challenge to better understand the wake stability for these so-called mixed convection flows, more insight into the influence of heat input is of practical importance e.g. for electronics cooling and for the design of compact heat exchangers. However, in comparison to the forced convection case, the wake characteristics of a heated cylinder have hardly been investigated. In the early 1970s, the effect of heat input was studied to determine the influence on the mean heat transfer coefficient. This information was needed to improve the quality of hot-wire velocity measurements. More detailed studies were carried out in the 1980s. For a vertically upward flow past a horizontal cylinder, an increase of the cylinder wall temperature results in an increase of the natural shedding frequency (Badr 1984; Noto, Isidea & Matsumoto 1983; Noto & Matsumoto 1987). However, above a critical heat input vortex shedding is suppressed. For this heat input the vortex street converts to a steady wake flow in which two twin vortices are situated. A further increase of the heat input causes these vortices to disappear, resulting in a thermal plume (Michaux-Leblond & Bélorgey 1997). Here the dualism between buoyancy and viscous effects was considered to be the source of the sudden disappearance of the vortex shedding phenomenon.

Even more interesting is the situation where the heated horizontal cylinder is exposed to a non-vertical cross-flow. The non-parallelism between the cross-flow direction and the buoyant force causes the flow pattern to become asymmetric, with the vortices in the upper vortex row having slightly different characteristics than the vortices in the lower row. The effect of the angle between the main flow direction and the gravitational vector was numerically investigated by Noto (1990). From this study it was found that the angle of attack has a major influence on the vortex street characteristics. Starting with an angle of 180° (corresponding to a vertical upward flow) it was found that first the vortex shedding was suppressed by increasing heat addition. When the angle of attack was decreased, the wake became periodic again, while for angles smaller than 90°, the natural frequency was found to become even larger than for the unheated situation. Unfortunately, the processes responsible for the observed change in the wake characteristics were not explained. Besides, in Noto's study only the near-wake effects were evaluated; downstream effects of the induced heat were not discussed.

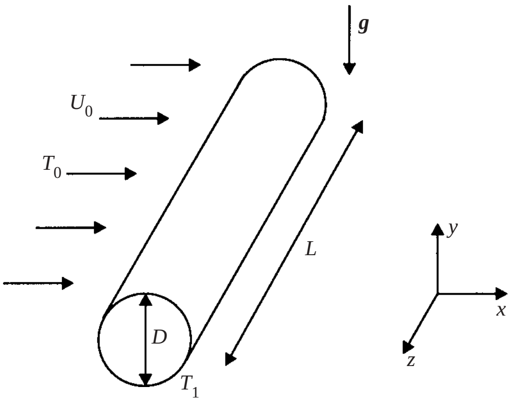

FIGURE 1. Problem definition.

In the present study the effect of heat input on the vortex structures and the wake characteristics is investigated for a horizontal cylinder exposed to a horizontal cross-flow. The Reynolds number with respect to the cylinder diameter is fixed at a value of 75, which is considered to be a reference case for vortex shedding behind an unheated cylinder. The work of Green & Gerrard (1991) discusses in detail the vortex shedding mechanism for this case. Furthermore, for a Reynolds number of 75 and without heat input the flow is fully two-dimensional. The heat input in the present study is restricted so that no early thermally induced collapse of the vortex street takes place. This problem is investigated both numerically and experimentally. In § 2 the problem definition is given together with the equations that describe it. The experiments were performed in a towing tank, in which the flow characteristics were measured by using high-resolution particle velocimetry (HiRes-PV). Both the experimental set-up and the HiRes-PV technique are described briefly in § 3. For the numerical study a spectral element method was employed, allowing calculation of the flow field with a high accuracy. In § 4 a brief introduction is given to this method. The effect of heat input on the wake characteristics and the behaviour of the vortex structures further downstream is discussed in § 5, while a detailed description of the effect of heat on the vortex shedding process is presented in § 6. Finally, some conclusions are formulated in § 7.

2. Problem definition and equations

The problem under consideration (figure 1) consists of a horizontal cylinder with outer diameter D and length L, heated to a constant temperature T_1 and placed in a uniform horizontal cross-flow with velocity U_0 and fluid temperature T_0. The flow is described in terms of a Cartesian x, y, z-coordinate system, with x pointing in the (horizontal) direction of the main flow, z pointing in the spanwise direction, while the y-direction is vertically upwards (antiparallel with the gravitational acceleration).

For small temperature differences the Boussinesq approach can be applied. By scaling the velocities by U_0, the spatial coordinates by D, the time by D/U_0, the pressure by ρU_0^2, the temperature by ΔT (with $\Delta T = T_1 - T_0$) and the gravitational acceleration by its magnitude g, the flow can be described by the dimensionless conservation equations for mass, momentum and heat:

$$\nabla\cdot\boldsymbol{u}=0, \tag{2.1}$$

$$\frac{\partial \boldsymbol{u}}{\partial t}+\boldsymbol{u}\cdot\nabla\boldsymbol{u}=-\nabla p+\frac{1}{Re_D}\nabla^2\boldsymbol{u}-Ri_D\Theta\boldsymbol{g}, \tag{2.2}$$

$$\frac{\partial \Theta}{\partial t}+\boldsymbol{u}\cdot\nabla\Theta=\frac{1}{Re_D Pr}\nabla^2\Theta, \tag{2.3}$$

with $\boldsymbol{u}$, $\Theta=(T-T_0)/\Delta T$, p and $\boldsymbol{g}$ the dimensionless velocity vector, temperature, pressure and gravitational vector, respectively. In these equations the following non-dimensional numbers appear: the Reynolds number $Re_D=U_0D/\nu$, the Richardson number $Ri_D=g\beta\Delta TD/U_0^2$ and the Prandtl number $Pr=\nu/\alpha$, with α the thermal diffusity, ν the kinematic viscosity and β the thermal expansion coefficient.

As already mentioned, in the present study the Reynolds number is kept constant at a fixed value of 75. The Richardson number, expressing the relative importance of the buoyancy forces and the inertia forces, is varied between 0 and 1. In the present experiments this corresponds with temperature differences in the range $0<\Delta T<5$°C. For these Ri_D the flow behind the cylinder is highly influenced by the shed vortex structures, which for $Ri_D=0$ form a von Kármán vortex street.

By taking the curl of the momentum equation one derives the vorticity equation. Assuming a two-dimensional flow in the (x, y)-plane, the vorticity vector $\boldsymbol{\omega}$ is directed in the z-direction, i.e. $\boldsymbol{\omega}=(0,0,\omega_z)$. The vorticity equation then reduces to a scalar transport equation, written as

$$\frac{\partial \omega_z}{\partial t}+\boldsymbol{u}\cdot\nabla\omega_z=\frac{1}{Re_D}\nabla^2\omega_z+Ri_D\frac{\partial\Theta}{\partial x}, \tag{2.4}$$

with ω_z the out-of-plane component of the vorticity vector $\boldsymbol{\omega}$, defined as

$$\omega_z=\frac{\partial v}{\partial x}-\frac{\partial u}{\partial y}. \tag{2.5}$$

The second term on the right-hand side of (2.4) is the so-called baroclinic production term, representing production of vorticity within the flow domain due to a non-zero component of the temperature gradient perpendicular to $\boldsymbol{g}$. In contrast to the case of iso-thermal flow, heat addition can cause the total circulation of the flow to change.

3. Measurements

3.1. *Experimental set-up*

A towing tank construction has been designed which allows detailed experiments on the flow behind the cylinder. In this construction the cylinder is towed through the water tank (figure 2). The cylinder, with diameter $D=8.5$ mm and length $L=495$ mm, is kept in position by two Perspex plates (figure 2*b*) with dimensions length × width × height = 50 cm × 0.4 cm × 65 cm. The plates are connected to a stiff structure, carrying the cylinder and the measuring equipment. The carrier can move at a prescribed constant speed (for $Re_D=75$ the speed equals 8.9 mm s^{-1} at an ambient temperature of 20°C) along two guiding rails, mounted on top of the tank. To move the carrier an electromotor is used. The motor is coupled to the drive-wheel by a 1:100 gear and is corrected for its variation in rotational speed by means of a closed circuit, resulting in a variation in the rotational speed of less than 0.2%. An almost inelastic belt is used for the coupling between the electromotor and the carrier system. Due

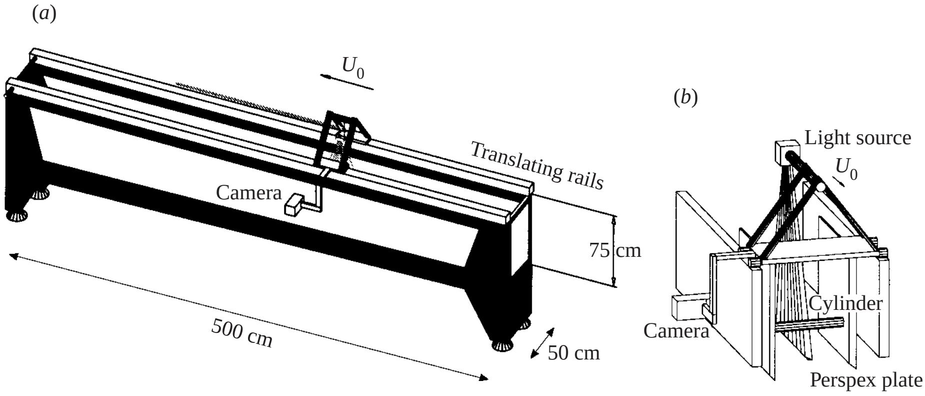

FIGURE 2. Towing tank construction: (*a*) overview of the towing tank (the arrow indicates the translation direction of the carrier system), (*b*) carrier system.

to inaccuracies in the translation speed of the carrier and variations in the ambient temperature the inaccuracy in the Reynolds number is estimated to be ± 1.

The specific dimensions of the towing tank are length × width × height = 500 cm × 50 cm × 75 cm (figure 2*a*). By choosing $Re_D \approx 75$, the length of the tank allows measurement of about 60 characteristic shedding periods of the specific flow problem. The distance between the end plates (equal to the length of the cylinder) is chosen such that the relative thickness of the boundary layers along the carrying plates (figure 2*b*) is small. For $Re_D \approx 75$ the thickness of these boundary layers at the position where the cylinder is clamped to the Perspex plates is at maximum about a few percent of the cylinder span. Any direct influence of the boundary layer on the vortex shedding in the cylinder wake in the centre of the tank can therefore be neglected. An indirect influence, such as oblique vortex shedding (Williamson 1989) may still be present. However, we found that this oblique shedding is suppressed by the end plates between which the cylinder is clamped, by performing visualization experiments using an electrolytic precipitation method.

Due to small temperature variations in the laboratory, even after long waiting periods between the preparation and the actual start of an experiment, weak residual flows could still be observed. The maximum velocities associated with these so-called background flows were measured to be approximately 0.2 mm s^{-1}. More information about the measuring device, its accuracy, and the measurement procedure can be found in Kieft, Rindt & van Steenhoven (1999).

3.2. *High-resolution particle tracking*

For the two-dimensional experiments a hybrid measurement technique combining particle tracking velocimetry (PTV) and particle image velocimetry (PIV) is used, a so-called high-resolution particle velocimetry method (HiRes-PV). The main step in a PTV method is the matching of particles in one frame with candidate particles in the next frame. In the HiRes-PV method the matching algorithm is improved by executing a PIV step on the acquired images. As a result, about 7000 to 10 000 independent velocity vectors (figure 3) can be determined using a $1k \times 1k$ camera. This gives significant improvement of the spatial resolution compared to more conservative techniques such as PIV or PTV. A more detailed description of the relevant algorithm parts and a test on the performance of the algorithm on real fluid flow data is presented by Bastiaans, van der Plas & Kieft (2001).

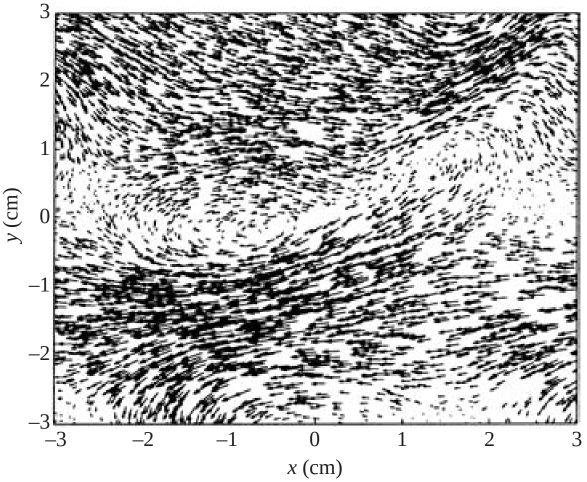

FIGURE 3. Characteristic result obtained with the HiRes-PV method. Note that the x- and y-coordinates here are indicated in cm.

Despite this high yield one should keep in mind that in the present study attention is mainly focused on the wake structures in the near and far wakes. The domain dimensions in focus at the camera are typically $20D \times 20D$. The length scale of the structures under consideration is around $1D$ whereas the boundary layer around the cylinder has a typical thickness of $0.1D$. Therefore, it is not surprising that the resolution of the velocity measurements presented here is too low to resolve the strong gradients in the boundary layers. This, in turn, results in large differences between the experimentally (see figure 5) and numerically (see figure 15) obtained vorticity fields in the vicinity of the cylinder wall.

3.3. *Data processing*

In principle the measured velocity field is an unstructured field. To calculate derived quantities such as vorticity or divergence, the unstructured field is transformed onto a structured grid. For this transformation a Gaussian weighting method is used (Agui & Jimenez 1987) which interpolates the random distributed vector field onto a regular grid. The interpolation error is strongly dependent on the ratio between the smallest wavelength of the flow and the average minimum distance between two neighbouring vectors. In the present experiment this ratio is about 50, resulting in an interpolation error of $\pm 0.5\%$ of the maximum velocity value.

The vorticity component ω_z is calculated from the interpolated data on the structured grid by using a first-order central difference scheme. In order to minimize the effect of random errors the vorticity fields are averaged over 6 samples (0.25 s). For the two-dimensional problem investigated, where the typical time scale is approximately 6 s (one shedding period), it is presumed that this averaging does not influence the observed results.

From the two-dimensional vorticity field some properties of the vortex structures can be derived. In order to assess the strength of a vortex in the flow field, the circulation Γ around a closed contour is calculated from

$$\Gamma = \int_A \omega_z \, \mathrm{d}A, \qquad (3.1)$$

with A the area enclosed by the iso-vorticity contour $C(\omega_a)$. Clearly, the value of the circulation calculated in this way will be affected by viscous effects. During the downstream advection of a structure the amount of vorticity initially confined by the contour $C(\omega_a)$ is spread by diffusion and some ends up outside the area A. This causes the calculated Γ to decrease, even though the vortex may be of constant strength. As viscous diffusion is hardly affected by buoyancy effects, the viscous spreading is assumed to be similar for all Ri_D. Hence, Γ can still be used to represent the vortex strength and to compare the results at different Ri_D.

For the position of the structure, the vorticity centroid is used, its coordinates being defined by

$$X = \frac{1}{\Gamma}\int_A \omega_z(x, y)x\,\mathrm{d}A, \qquad Y = \frac{1}{\Gamma}\int_A \omega_z(x, y)y\,\mathrm{d}A.$$

The value set for ω_a may affect the calculated values of X and Y. For example, for a too small value of ω_a experimental noise influences the calculated centroid position. On the other hand, for increasing values of ω_a the calculated centroid approaches the position of the vorticity extrema. In the present investigation, the closed iso-vorticity contour ω_a was set to $|\omega_a| = 0.2\omega_0$, with $\omega_0 = U_0/D$. This value of ω_a corresponds to about 10% of the maximum vorticity value just after the formation of the vortex structures. The accuracy in X and Y is a function of the downstream position because diffusion causes the vortices to widen, resulting in larger structures with lower peak values. Consequently, the calculated positions become less accurate and vary by from ± 0.1 at $x = 7$ to ± 0.25 at $x = 20$.

4. Numerical method

Parallel to the experiments, two-dimensional numerical simulations were performed. For an efficient temporal discretization of the Boussinesq equations (2.1) to (2.3), the (non-) linear convection–diffusion equations are split. This splitting operation is performed by applying a suitable integration factor (Maday, Patera & Ronquist 1990). As a result, a diffusion and a convection equation remain which can be discretized separately. The convection equation is temporally discretized by applying a three-step explicit Taylor–Galerkin scheme. The diffusion equation is discretized by an implicit second-order backwards difference scheme. The pressure term, arising in the diffusion equation as a kind of source term, is treated by an approximate projection scheme (Timmermans, Minev & van de Vosse 1996). The numerical scheme was validated by a study of the flow in a differentially heated cavity at intermediate and transitional Rayleigh numbers (Minev *et al.* 1996). The results are in very good agreement with other available numerical solutions.

For the spatial discretization a high-order spectral element method (SEM) is used which can be considered as a mixture of a finite element method (FEM) and a spectral method. The SEM combines the advantages of the other two methods. The principle is relatively straightforward. Within a small domain inside the fluid, a so-called element, the equations are discretized by using a spectral method. Combining the solutions obtained in all these elements finally results in the solution on the entire domain. Of course, special consideration has to be given to the continuity of the solution over the element boundaries. This decomposition of the domain into elements gives the method the geometric flexibility which can also be found in the finite element method. By using high-order approximation functions within such an element, a spectral convergence rate and small numerical errors, such as numerical

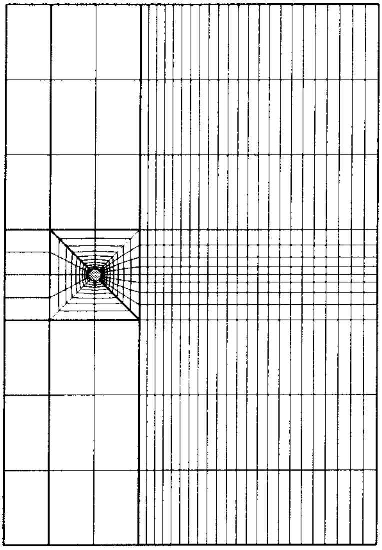

FIGURE 4. Spectral element grid consisting of 504 elements and 41238 nodal points (ninth-order approximation polynomial).

BC_{upper}	$\partial u/\partial n=0$	$v=0$	$\Theta=0$	$\partial q/\partial n=0$
BC_{lower}	$\partial u/\partial n=0$	$v=0$	$\Theta=0$	$\partial q/\partial n=0$
BC_{out}	$\partial u/\partial n=0$	$\partial v/\partial n=0$	$\partial\Theta/\partial n=0$	$\partial q/\partial n=0$
BC_{in}	$u=U_0$	$v=0$	$\Theta=0$	$\partial q/\partial n=0$
BC_{cyl}	$u=0$	$v=0$	$\Theta=1$	$\partial q/\partial n=0$

TABLE 1. Boundary conditions for upper, lower, outlet and inlet boundaries and cylinder wall. $\partial/\partial n$ denotes the normal derivative. Note that at one point at the outflow boundary $q=0$ is prescribed (see main text).

dispersion and diffusion, can be found. More information about validation of the numerical scheme can be found in Timmermans *et al.* (1996).

The element distribution used in the calculations is shown in figure 4. Within each element a ninth-order approximation polynomial is used resulting in more than 40 000 nodal points. A refinement study revealed that calculated quantities like wall vorticity, boundary layer thickness, position of the separation points and Strouhal number did not appreciably change when even finer grids were used. Also, computed values of the mean position of the separation points (119.3° for the upper wall and 240.7° for the lower wall) and the Strouhal number (0.1527) compare quite well with values presented in literature. A detailed study on the influence of the domain height (Kieft 2000) has revealed that for values larger than $48D$ almost no influence of the upper and lower boundaries is observed. The length of the domain has no significant influence as long as the domain inlet is more than $8D$ upstream of the cylinder. The total length of the computational domain equals $33D$.

The prescribed boundary conditions are presented in table 1. At the inlet and the cylinder wall Dirichlet boundary conditions are applied for both velocity components and the temperature. The normal velocity at the horizontal boundaries is set to zero ($v=0$), which, in combination with $\partial u/\partial n=0$, implies a zero tangential stress ($\sigma_t=0$) at these boundaries. Also, the temperature is set to zero here. At the domain outlet homogeneous Neumann conditions are prescribed for the normal and the tangential velocity components as well as for the temperature. The boundary conditions for the pressure correction term q (related to the defect in divergence freedom of the velocity field as calculated in a predictor step, see Timmermans *et al.* 1996) follow immediately from the global mass conservation and are $\partial q/\partial n = 0$. Because the pressure correction term is a solution of a Poisson equation with a Neumann boundary condition, at one point located on the domain outlet the Dirichlet condition $q = 0$ is prescribed. In combination with the conservation of mass this implicitly states that the pressure p is near zero at the outflow boundary (Timmermans *et al.* 1996). It should be noted that the vortices leaving the computational domain will be influenced by the applied boundary conditions at the outlet. However, from a study by van de Vosse, Minev & Timmermans (1995) it appeared that this influence is rather small. However, the results are presented up to $x = 22$ whereas the outlet boundary is positioned at $x = 25$.

5. Wake behaviour

The effect of heat on the vortex wake has been studied by considering the trajectories of the wake structures and the relative motions of the structures. This study was carried out both numerically and experimentally.

5.1. *Vortex trajectories*

Starting with the experimental results, the behaviour of the shed vortex structures within the cylinder wake was analysed for several shedding periods. The interrogation window of these experiments was fixed with respect to the cylinder and occupies the area between $x = 0$ (the cylinder position) and $x = 25$. For a duration of 120 s, the vortex positions were calculated from the measured velocity field at intervals of 1 s. Results are shown in figure 5(*b*, *d*, *f*) for $Ri_D = 0$, 0.5 and 1. These graphs show the trajectories of about 40 shed vortex structures (typical shedding period is 6 s). For both the upper and lower rows an exponential function, representing the average trajectory, is fitted through the vortex positions. The graphs on the left (figure 5*a*, *c*, *e*) show the vorticity contours for increasing Ri_D.

For $Ri_D = 0$, the shed vortices form a regular von Kármán vortex street. The average trajectories of the upper and lower vortices (figure 5*b*) show an almost symmetric profile with respect to the wake axis ($y = 0$). For increasing downstream position, both trajectories are deflected equally from the wake axis. This deflection can be seen as a widening of the vortex street due to viscous spreading of the vortex cores (Green & Gerrard 1991). For $Ri_D > 0$ (figure 5*d*, *f*) an additional deflection of the vortex trajectories in the negative y-direction is found. Keeping in mind the effect of buoyancy, one would intuitively expect the opposite, i.e. an upward deflection. This additional negative deflection is larger for $Ri_D = 0.5$ than for $Ri_D = 1$.

The vortex trajectories can also be analysed using the numerical results for $Re_D = 75$, $Pr = 7$ and Ri_D between 0 and 1. For about four typical shedding periods, the vortex positions are calculated and presented in figure 6. In the absence of any heat input ($Ri_D = 0$) the vortex trajectories show a symmetric widening of the vortex street. This widening is slightly smaller than obtained from the experimental results. The influence of experimental imperfections, like the occurrence of a background flow, are thought responsible for this. For $Ri_D > 0$ both the upper and the lower vortex trajectories move downwards with respect to the vortex trajectory found for $Ri_D = 0$. The deflection of the lower vortex row is larger than the deflection of the upper vortex row. Furthermore, it is found that for $Ri_D > 0$ the trajectories start at a higher

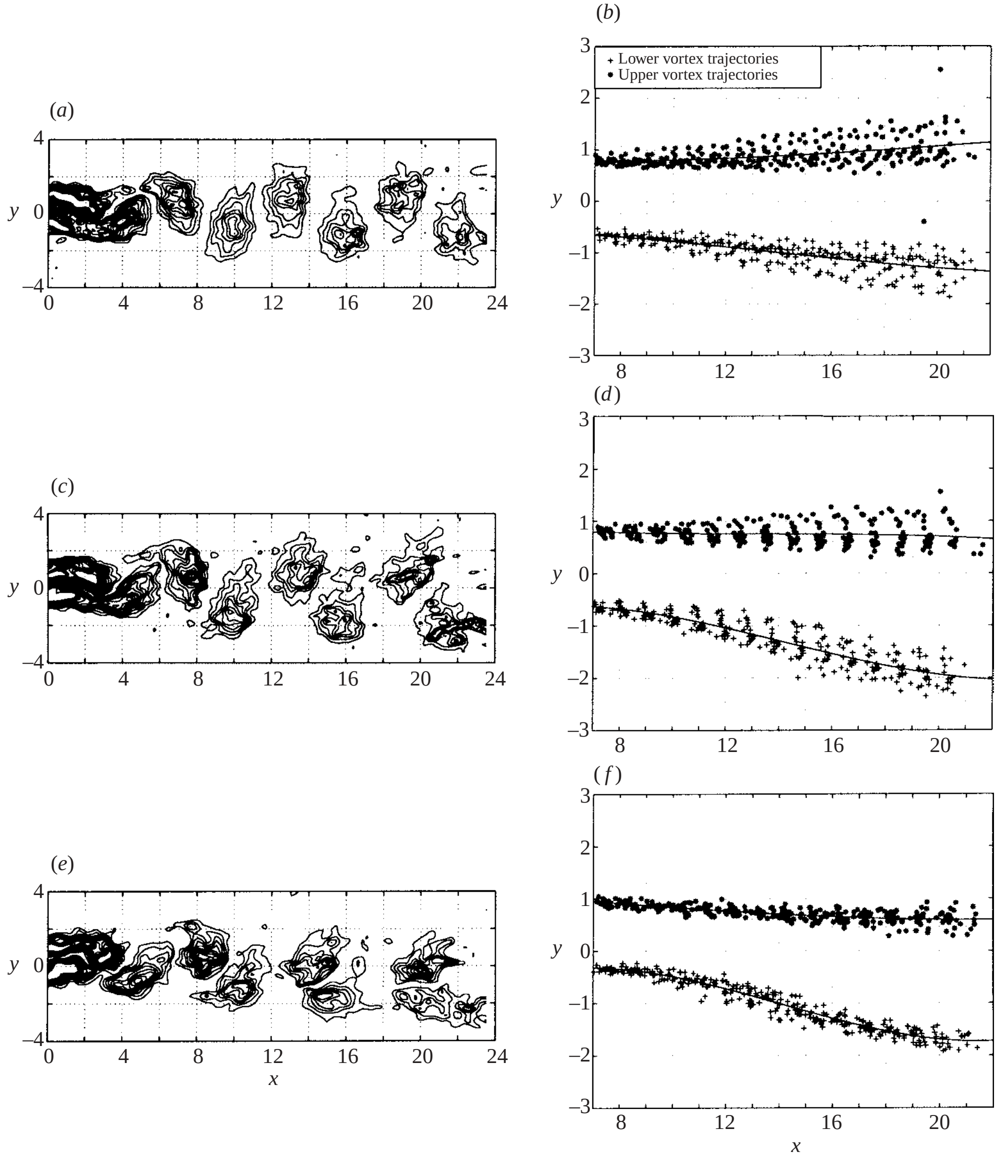

FIGURE 5. Experimental HiRes-PV results for $Re_D = 75$, showing vorticity contours at equivalent times for (*a*) $Ri_D = 0$, (*c*) $Ri_D = 0.5$ and (*e*) $Ri_D = 1$ and structure trajectories for (*b*) $Ri_D = 0$, (*d*) $Ri_D = 0.5$ and (*f*) $Ri_D = 1$.

y-position than for $Ri_D = 0$. This shift is assumed to be caused by heat effects in the near wake and can, although less pronounced, also be observed in the experimental results (compare figures 5*f* and 5*b*).

From the numerical results it appears that at the end of the domain the strongest deflection occurs for $Ri_D = 0.5$, see figure 6. For higher Ri_D-values, a less severe deflection was observed. To make a proper comparison one should take into account that for $Ri_D > 0$ the trajectories start at a higher y-position. To quantify the net deflection ΔY, the difference between the y-position of the vortex at $x = 22$ and its y-position just after formation at $x = 8$ has been determined (figure 6*b*). For

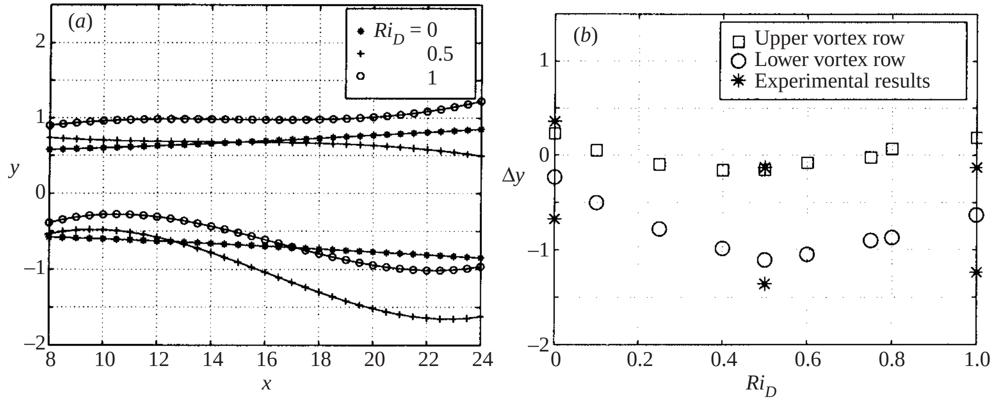

FIGURE 6. Calculated wake deflection for $Re_D = 75$ and varying Ri_D: (*a*) vortex trajectories and (*b*) net deflection $\Delta Y = y(x = 22) - y(x = 8)$.

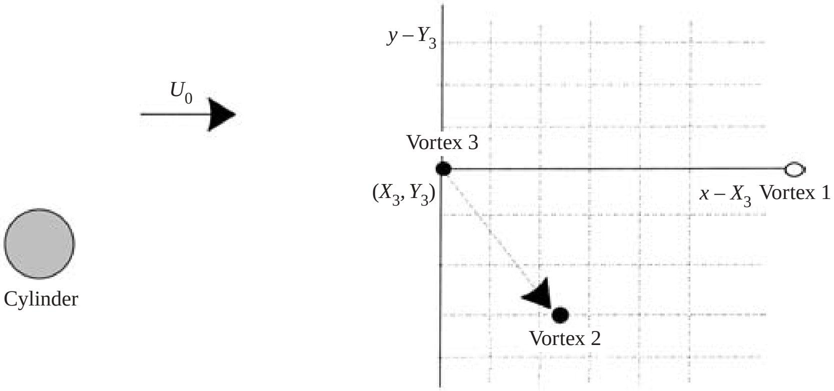

FIGURE 7. Reference frame attached to an upper vortex (Vortex 3) to analyse the relative motion of earlier-shed vortices (Vortices 1 and 2).

$Ri_D = 0$, ΔY is positive for the upper vortex row, expressing a deflection in the positive y-direction, and negative for the lower vortex row, representing a deflection in the negative y-direction. The value of the deflection for $Ri_D = 0$ is (in the absolute sense) the same for both rows. This observed deflection represents the widening of the vortex street. On increasing Ri_D, the lower vortex row moves in the negative y-direction. The strongest deflection is observed for $Ri_D = 0.5$. Further increase of Ri_D results in a less severe net deflection. For the upper vortex row, an increasing Ri_D also results in a downward deflection compared to the unheated situation. The largest difference with respect to the unheated situation is observed for $Ri_D = 0.4$, where the value of ΔY is negative. For higher heat input ΔY increases again.

5.2. *Vortex motion*

The relative motion of the structures during their downstream advection can be quantified by attaching a reference frame to one of the vortices in e.g. the upper row (see figure 7). For both the experiments and the computations the relative motion of an earlier shed lower vortex (Vortex 2) with respect to an upper vortex (Vortex 3) is determined in the region $x = 8$ to $x = 23$. The results for varying Ri_D-values are presented in figure 8.

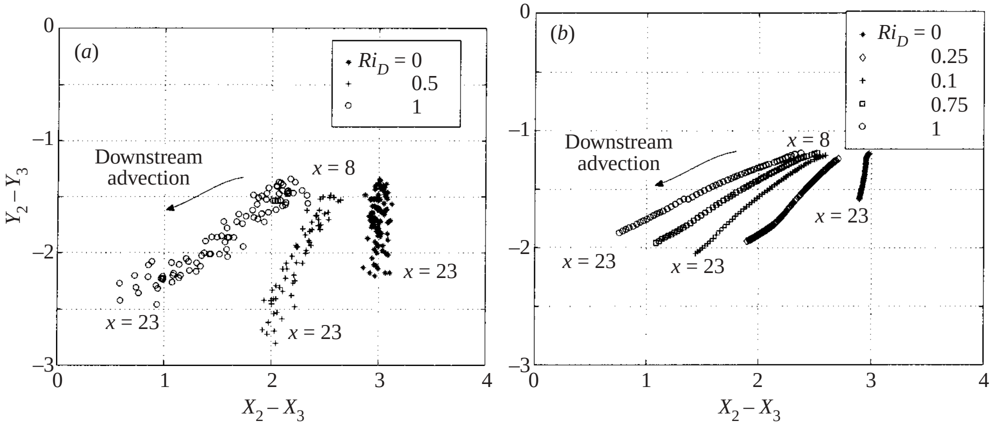

FIGURE 8. Relative motion of a lower vortex (Vortex 2) with respect to an upper vortex (Vortex 3) for $Re_D = 75$: (*a*) experimental results for $Ri_D = 0$, 0.5 and 1; (*b*) numerical results for $Ri_D = 0$, 0.25, 0.5, 0.75 and 1.

For $Ri_D = 0$ (figure 8*a*) the experimental results show that the lower vortex, starting at $((X_2 - X_3), (Y_2 - Y_3)) \approx (3, -1.3)$, moves in vertical direction away from the upper vortex to $((X_2 - X_3), (Y_2 - Y_3)) \approx (3, -2.2)$. In the vortex trajectory (figure 5*b*), this behaviour is observed as the widening of the vortex street. For the numerical results (figure 8*b*) a similar behaviour can be observed, although the widening is somewhat less. Also, the ratio between the vertical $(Y_3 - Y_2)$ and horizontal inter-vortex distance $(X_1 - X_3)$ can be determined, denoted here as a/b. For the experimental results this ratio varies as a function of the downstream position, namely from 0.23 at $x = 8$ to 0.33 at $x = 23$. The spacing ratio determined from the numerical simulations varies from 0.20 to 0.27.

For $Ri_D > 0$, a stronger relative motion between the structures is observed. Again the structures show an increasing separation in the y-direction as they move downstream. Compared to the forced convection case, this widening is about twice as high for all $Ri_D > 0$. This effect is more pronounced in the experimental than in the numerical results. Also interesting is the approach of the structures in the x-direction. For increasing Ri_D the lower vortex moves more into the direction of the upper one. In combination with the observed relative motion in the y-direction, it appears as if the lower vortex is slowly rotated underneath the upper vortex. This rotational drift hints at strength differences between the vortices in the upper and lower rows.

5.3. *Vortex strengths*

As a measure of the strength of a vortex structure its peak vorticity value is used. The spatio-temporal evolution of the strengths of the wake vortices is shown in figure 9 for $Ri_D = 0$, 0.5 and 1, for both the experiments and numerical simulations. For increasing Ri_D, the peaks of the negative upper vortices increase (in an absolute sense). In contrast, the lower vortex peaks do not show a strong dependence on Ri_D, implying an asymmetry in the wake. This asymmetry is already present just after the formation of the structures at $x = 8$. The numerical results show much higher (negative) values for the vorticity peaks than the ones measured. This is probably due to the lower resolution in the experiments than in the calculations. In the region of interest (the near and far wakes) the difference in resolution is at least a factor 3 in both the x- and y-directions.

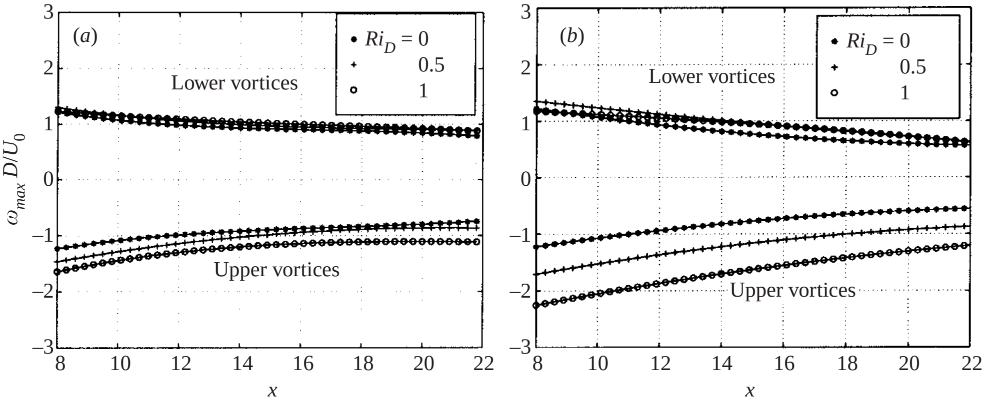

FIGURE 9. Absolute vorticity peaks for $Re_D = 75$ and varying Ri_D: (*a*) experimental results, (*b*) numerical results. Note that the lower structures have positive vorticity and the upper ones negative vorticity.

Ri_D	0	0.25	0.5	0.75	1
Γ_u	−2.45	−2.55	−2.66	−2.73	−2.83
Γ_l	2.45	2.37	2.20	2.11	2.00
$\Delta\|\Gamma\|/\Gamma_u$	0	0.07	0.18	0.23	0.29

TABLE 2. Numerical values for the structure strengths evaluated at $x = 12$. These values are used as input for the point-vortex simulations.

As well as the peak vorticity values, the circulation of the structures, as defined by (3.1), is also analysed. During the downstream advection of the structures, Γ is calculated for various vortex positions. It appeared that the heat supplied by the cylinder caused the upper vortices (negative Γ) to become stronger, while the lower vortices became weaker. The strength difference is quantified in table 2, which presents the difference in calculated strength between the upper and lower vortices at $x = 12$. For $Ri_D = 0$ the strength difference $\Delta|\Gamma| = |\Gamma_l| - |\Gamma_u|$ between the lower and upper vortices is zero, while for increasing Ri_D the quantity $\Delta|\Gamma|$ becomes more negative. This implies that for increasing heat input the upper vortex becomes stronger than the lower vortex.

5.4. *Point-vortex calculations*

The influence of the observed strength difference on the vortex street behaviour has been analysed using a point-vortex model. The model allows monitoring of the behaviour of a street of opposite-signed vortices in a uniform flow with velocity U_0. For the structure strength at the inlet of the computational domain ($x_{pv} = 0$, with the subscript referring to point vortex), the numerically determined strength at $x = 12$ is used (table 2). At this position it is assumed that the strength difference is at its maximum value. The strength decay is modelled by a prescribed exponential decrease as a function of the downstream position x. The spacing between the vortices entering the computational domain is set equal to the spacing according to the von Kármán stability criterion ($a/b = 0.281$).

For increasing strength difference the point-vortex simulations show an increasing deflection of both vortex rows in the negative y-direction (figure 10*a*). The deflection

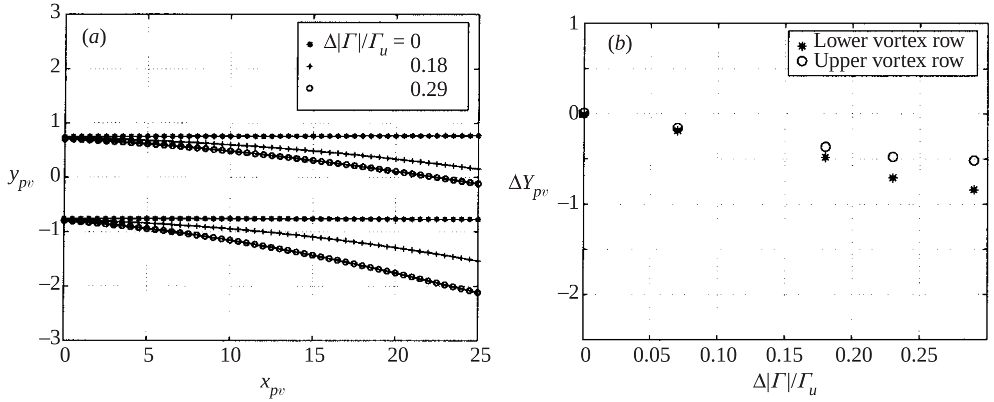

FIGURE 10. Calculated vortex wake deflection using the point-vortex model for varying $\Delta|\Gamma|$: (*a*) vortex trajectories and (*b*) net deflection $\Delta Y_{pv} = y_{pv}(x = 22) - y_{pv}(x = 8)$. The corresponding Ri_D values are given in table 2. Note that $x_{pv} = 0$ coincides with $x = 12$.

of the lower vortex row is larger (figure 10*b*), a behaviour also observed in the experimental and numerical results (see figure 6*b*). Further comparison of these results with the experimental and numerical ones shows that the point-vortex model gives an under-prediction of the deflection, probably due to the neglected size of the vortex cores. For example, from the numerical calculations a value of $\Delta Y \approx -1$ is found for the lower vortex row at $Ri_D = 0.5$, whereas $\Delta Y \approx -0.5$ in the point-vortex simulations for $\Delta|\Gamma|/\Gamma_u = 0.18$. However, if one subtracts the street widening as found in the numerical or experimental results for $Ri_D = 0$ ($\Delta Y = +0.25$ for the upper vortex row and $\Delta Y = -0.25$ for the lower vortex row, see figure 6*b*), the deflections as found with the point-vortex model become comparable, at least for $Ri_D < 0.5$. For higher values of Ri_D the experimental and numerical deflections decrease again, while the deflection as predicted by the point-vortex model increases continuously. This difference is probably caused by the growing influence of the buoyancy force for increasing Ri_D-values, which causes the vortices to move in the positive y-direction. This force is not incorporated in the point-vortex model.

From the vortex trajectories as calculated with the point-vortex model, the relative motion between two subsequent structures can be deduced (figure 11, see also figure 7). For $\Delta|\Gamma| = 0$ (or, equivalently, $Ri_D = 0$) almost no relative motion between these two structures occurs (this result is not presented in figure 11*b*). The widening of the vortex street for $Ri_D = 0$ observed in the experimental and numerical results is not represented by the point-vortex model. This supports the hypothesis that the vortex street widening is due to viscous spreading of the vortex cores (Green & Gerrard 1991), a mechanism which is – of course – not accommodated by the point-vortex model. As can be seen from figure 11(*b*), an increasing strength difference (equivalent to $Ri_D > 0$) again results in a rotational drift of the lower vortex around the upper vortex. For this situation, a vertical displacement of the vortices in the lower row, which can be seen as a widening of the vortex street, also appears in the point-vortex simulations. As it does not appear for $Ri_D = 0$, it can be concluded that the additional widening for $Ri_D > 0$ is caused by a non-zero $\Delta|\Gamma|$ and not by viscous spreading of the vortex cores. This almost entirely explains the additional widening for $Ri_D > 0$ of about $0.5D$ found in the experimental and numerical results (figure 8*a*, *b*).

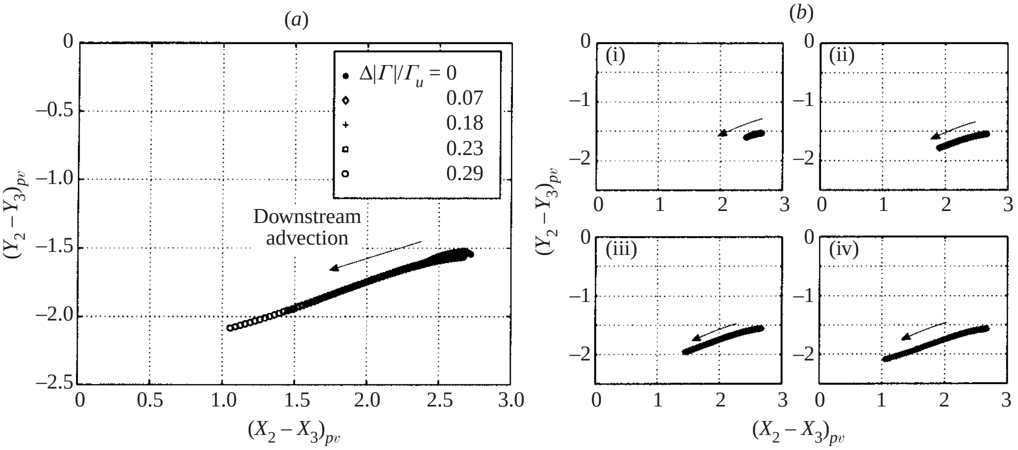

FIGURE 11. Relative motion of a lower vortex (Vortex 2) with respect to an upper vortex (Vortex 3) for increasing strength difference as calculated by the point-vortex model: (*a*) paths for different $\Delta|\Gamma|/\Gamma_u$, (*b*) paths plotted separately: (i) $\Delta|\Gamma|/\Gamma_u = 0.07$, (ii) 0.18, (iii) 0.23, (iv) 0.29. The motion of the vortices along the paths is indicated with an arrow. The corresponding Ri_D values are given in table 2.

It is interesting to observe that for all strength differences, the relative motion of the lower vortices is along the same path (figure 11*a*). However, for an increasing strength difference the length of this path increases (figure 11*b*). This cannot be observed in the numerical and experimental results of the real flow field (figure 8). In these results the direction of the paths changes for varying Ri_D. As mentioned above, the spacing between the vortices entering the computational domain in the point-vortex simulations ($x = 12$) is set equal to the spacing according to the von Kármán stability criterion ($a/b = 0.281$) for all values of $\Delta|\Gamma|$. In reality this spacing will vary. Therefore, in the experiments and the calculations, the interaction between the structures will be different for varying $\Delta|\Gamma|$ (varying Ri_D), probably resulting in the aforementioned change in path directions.

From the point-vortex simulations it can be concluded that the observed behaviour of the wake (deflection and relative vortex motion) is caused by the difference in strength between the upper and lower vortex rows. The analysis of the structure strengths shows that this strength difference is already present just after the formation (and shedding) of the vortex structures. Apparently, the origin of the strength difference between the upper and lower vortices lies in the formation process of the structures.

6. Near-wake vorticity sources

Within the near wake ($x < 6$) several processes may lead to a difference in strength between the vortices. When considering the local change of vorticity two sources can be distinguished: diffusion and advection of wall vorticity to the interior of the flow and thermally induced baroclinic vorticity production, represented by the second and third terms and by the fourth term in (2.4), respectively. These sources have been analysed using the detailed results of the numerical simulations. Furthermore, the numerical results allow monitoring of additional quantities such as transport of vorticity.

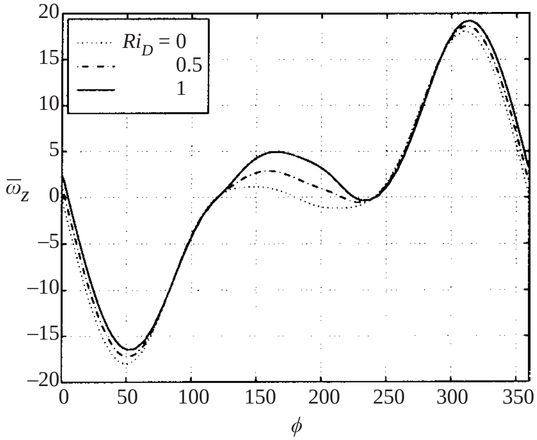

FIGURE 12. Numerically calculated period-averaged wall vorticity $\overline{\omega_z}(r = R, \phi)$ for $Re_D = 75$ and varying Ri_D.

6.1. *Wall vorticity*

The effect of heat on the wall vorticity will be elucidated by considering the period-averaged wall vorticity $\overline{\omega_z}$, which is defined as

$$\overline{\omega_z}(r = R, \phi) = \frac{1}{T} \int_0^T \omega_z(r = R, \phi, t)\,\mathrm{d}t, \tag{6.1}$$

with T here representing the shedding period, R the radius of the cylinder and ϕ the angle indicating the position on the cylinder wall (measured in a clockwise direction from the most upstream point on the cylinder wall).

As can be seen in figure 12, an increasing Ri_D-value causes the level of the negative vorticity on the upper side of the cylinder ($0 < \phi < 120°$) to become lower. Between the two separation points ($120° < \phi < 240°$) positive wall vorticity is added to the flow. Upstream of the lower separation point ($240° < \phi < 360°$) the wall vorticity also increases (becomes less negative). Apparently, addition of heat causes the negative wall vorticity to decrease and the positive to increase. As a consequence, one would expect that advection of wall vorticity causes the strength to decrease for the upper vortices and to increase for the lower vortices. This wall effect counteracts the tendency of the upper vortices to become stronger (more negative) than the lower ones when heat is added.

The asymmetry in the vorticity distribution around the cylinder results from the different action of heat in the upper and lower boundary layers. Inspection of the near-wall velocity profiles revealed a decrease in the tangential velocity in the upper boundary layer and an increase in the lower one. For the pressure the opposite was seen, i.e. a higher pressure in the upper boundary layer and a lower pressure in the lower one. This pressure difference, in turn, results in a net lift force acting on the cylinder. Since the present study focuses on the influence of a heat input on the wake structures behind the heated cylinder rather than the boundary layer characteristics around the cylinder, this aspect will not be discussed any further here.

6.2. *Baroclinic vorticity production close to the cylinder wall: $x < 1$*

The second source of vorticity is due to baroclinic production, represented by the term $Ri_D \partial\Theta/\partial x$ in (2.4). Considering the schematic temperature distribution around

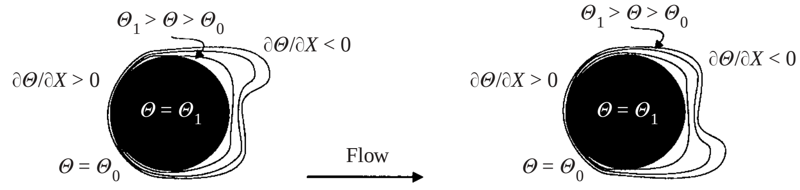

FIGURE 13. Schematic representation of the qualitative behaviour of the baroclinic vorticity production close to the cylinder wall at two out-of-phase moments in time. Θ indicates the dimensionless temperature.

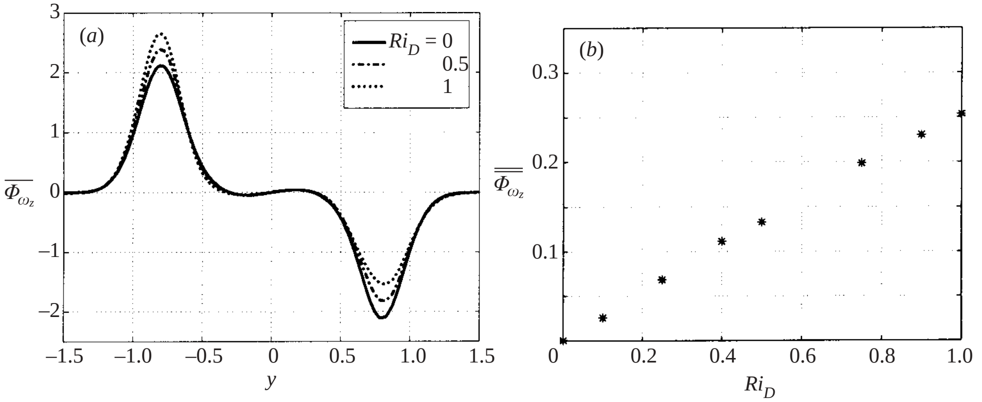

FIGURE 14. The effect of heat addition on the period-averaged vorticity flux $\overline{\Phi_{\omega_z}}$ for $Re_D = 75$ and varying Ri_D: (*a*) through a cross-section at $x/D = 1$, (*b*) integrated over the cross-section height.

the cylinder shown in figure 13 one can easily deduce the sign of this production term. At the upstream side, the temperature decreases for decreasing x-values, resulting in a positive $\partial\Theta/\partial x$ and, consequently, a positive vorticity production. This production of vorticity is expected to be about constant during one shedding period. On the rear side the opposite occurs, resulting in a negative production of vorticity. During the shedding cycle, the value of this negative production term varies strongly. The net effect of the baroclinic vorticity production close to the cylinder wall cannot, therefore, easily be deduced.

By considering the local period-averaged flux of vorticity at the vertical cross-section $x = 1$, defined as

$$\overline{\Phi_{\omega_z}}(x = 1, y) = \frac{1}{T}\int_0^T u\omega_z(x = 1, y, t)\,\mathrm{d}t, \tag{6.2}$$

one may estimate the cumulative effect of the baroclinic vorticity production close to the cylinder wall and the advection of wall vorticity. This quantity approximately describes how much vorticity produced upstream from the cross-section $x = 1$ can potentially be captured in the shed vortex structures.

A graphical representation of this vorticity flux as a function of y is given in figure 14(*a*). It can be concluded that an increasing Ri_D-value causes the local flux of negative vorticity to decrease (upper wake-half), while the flux of positive vorticity increases (lower wake-half). The total period-averaged vorticity flux $\overline{\overline{\Phi\omega_z}}$ transported over the boundary $x = 1$ can be calculated by integrating the local vorticity flux

$\overline{\Phi_{\omega_z}}(x = 1, y)$ over the entire cross-section height

$$\overline{\overline{\Phi_{\omega_z}}}(x = 1) = \int_{-12D}^{12D} \overline{\Phi_{\omega_z}}(x = 1, y)\,\mathrm{d}y. \tag{6.3}$$

This net vorticity flux (shown in figure 14*b*) increases linearly with increasing Richardson number. So, addition of heat results in more positive than negative vorticity entering the region $x > 1$. From the results on the local and total period-averaged flux of vorticity it can, therefore, be concluded that the observed difference in strength between the upper and lower vortex structures is not caused by vorticity sources in the vicinity of the cylinder.

6.3. *Baroclinic vorticity production in the near wake:* $1 < x < 6$

The structure formation is further analysed in the downstream region $1 < x < 6$. Here the situation changes completely, as can be easily observed from the sequence of graphs given in figure 15, representing the spatial distribution of vorticity (figure 15*a*, *c*, *e*, *g*, *i*, *k*) and the baroclinic vorticity production (figure 15*b*, *d*, *f*, *h*, *j*, *l*).

From the vorticity production graphs it can be seen that when an upper vortex is initiated at $t/T = 0$ (figure 15*a* at $x \approx 1.7$, $y \approx 0.5$), an area of negative baroclinic vorticity production is located at the tip of the (negative) vorticity strand (figure 15*b* at $x \approx 1.7$, $y \approx 0.5$). The production term therefore contributes to the vortex structure to be formed. Slightly upstream at $x \approx 1$, $y \approx 0.5$, a small area of positive production can be found. This area coincides with the area where somewhat later the constriction of the vorticity strand takes place. While the area of positive production almost disappears (figure 15*d*), the negative one is growing in size and strength (figure 15*d*, *f*, *h*). Therefore, in the first half of the formation period the production term adds to the newly formed negative upper structure. In the second half, the area of positive vorticity production just upstream of the negative production becomes almost as strong as the negative production. It is then expected that the absolute strength of the vortex structure formed is no longer much influenced by these production terms.

During the formation of a lower vortex (figure 15*h*, *j*, *l*), again an area of negative and positive vorticity production is located in the region where the new vortex structure is formed (figure 15*h* at locations $x \approx 1.6$, $y \approx -0.3$ and $x \approx 1$, $y \approx -0.2$, respectively). Especially in the early stage of the vortex formation process (between $1 < x < 3$, figure 15*h*, *j*) the production of negative vorticity is stronger. Therefore, in the first half of the formation process, a net amount of negative vorticity is produced within the lower vortex. This production causes the lower vortex to become weaker compared to the situation for $Ri_D = 0$. In the second half of the vortex formation process, the production of positive vorticity within the newly formed structure increases and becomes more or less equal to the contribution of the negative production, resulting in no net change of vortex strength.

The quantitative contributions of the baroclinic vorticity production to the circulation of the structure can be analysed by integration of the baroclinic vorticity production term over a confined area. For the production term Γ_{prod} one then can write

$$\Gamma_{prod} = \int_A Ri_D \frac{\partial \Theta}{\partial x}\,\mathrm{d}A, \tag{6.4}$$

where the area A is bounded by the threshold production level $|Ri_D(\partial\Theta)/(\partial x)| = 0.1$. The integrated productions of the positive areas as well as the negative areas are plotted separately for the upper vortex in figure 16(*a*) as a function of their

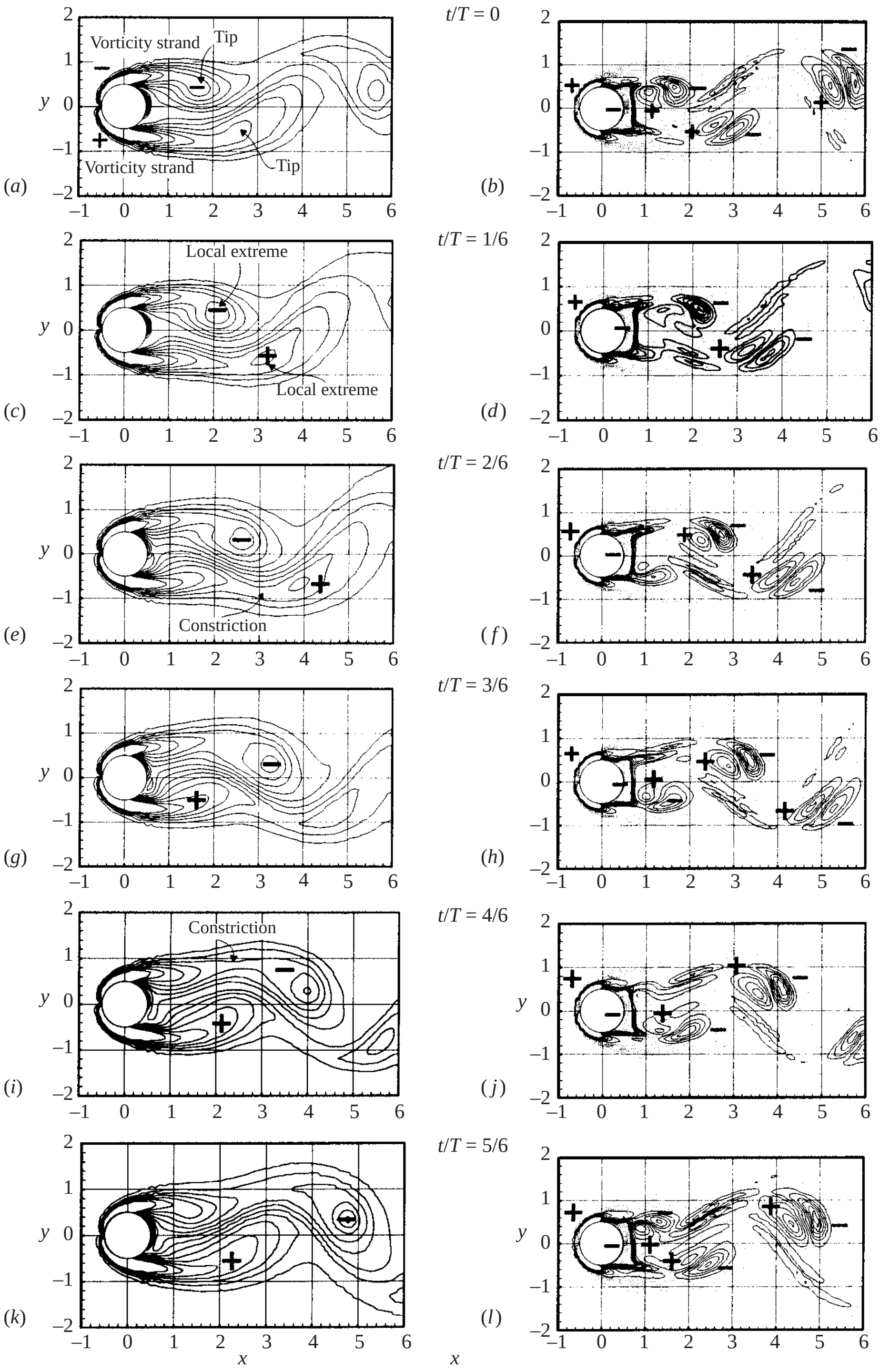

FIGURE 15. Numerically calculated near-wake vorticity (left: a, c, e, g, i, k) and vorticity production (right: b, d, f, h, j, l) for $Re_D = 75$ and $Ri_D = 0.5$. The vorticity production graphs are drawn together with the vorticity distribution (dashed lines). The time position within a shedding cycle is indicated in the middle.

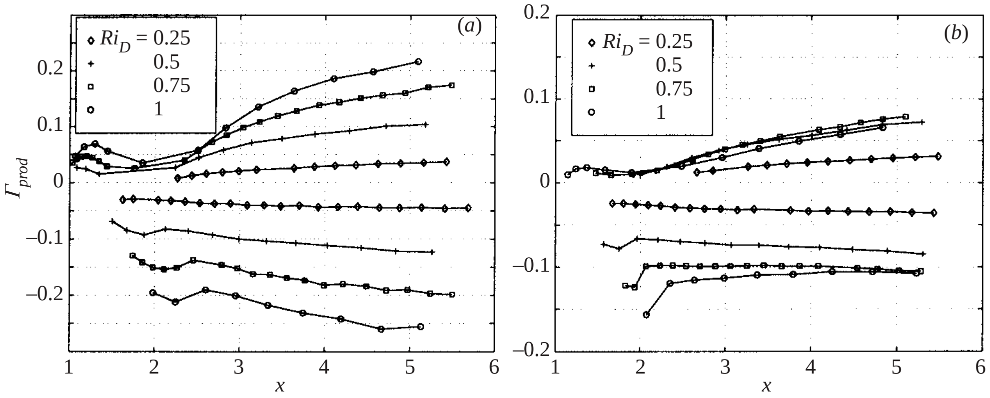

FIGURE 16. Integrated vorticity production Γ_{prod} for $Re_D = 75$ and varying Ri_D: (*a*) in the upper vortex and (*b*) in the lower vortex.

downstream position. It can be seen that for $x < 4$ the negative vorticity production is significantly larger than the positive vorticity production. Especially in the region $1 < x < 3$, the positive production is relatively small, resulting in only a negative vorticity contribution to the structures. Besides, the contour plots presented in figure 15 have shown that the area of positive vorticity production does not fall within the vortex structure and does not directly contribute to the structure strength. In the region $x > 4$ the positive vorticity production increases and becomes as strong as the negative vorticity production at $x \approx 5$. At this downstream position the positive vorticity production area also falls within the vortex structure, and, therefore, contributes to the vortex strength.

For the lower structure, the integrated vorticity production term Γ_{prod} shows a similar behaviour (figure 16*b*). Again, the negative vorticity production is stronger than the positive vorticity production. The positive vorticity production remains negligible up to $x \approx 2$. Beyond this point, the positive vorticity production increases but remains smaller than the negative vorticity production within the scope of figure 16(*b*).

The contribution of the production term to the vortex strength can also be deduced from the downstream development of the peak (in an absolute sense) values of vorticity (figure 17*a*)†. The initial values of these extremes for the upper row are almost the same for all Ri_D values. However, in the downstream area $1.5 < x < 3$, these, values decay significantly slower when heat is added to the cylinder ($Ri_D > 0$) compared to the unheated cylinder ($Ri_D = 0$). For $Ri_D = 1$ even an increase in extreme vorticity is found. In the downstream area $x > 4$ the behaviour of the negative vorticity peaks is quite similar for all Ri_D values. This also holds for the positive vorticity peaks of the lower vortex row but now for the whole downstream area. From this observation it can be concluded that during the vortex generation the baroclinic vorticity production contributes to the upper vortex and makes almost no net contribution to the lower vortex. In summary, it can be stated that the observed strength difference is caused by the baroclinic-vorticity production in the downstream area $1.5 < x < 4$.

---

† In figure 9(*b*) the same quantity is plotted but for the downstream region $8 < x < 22$.

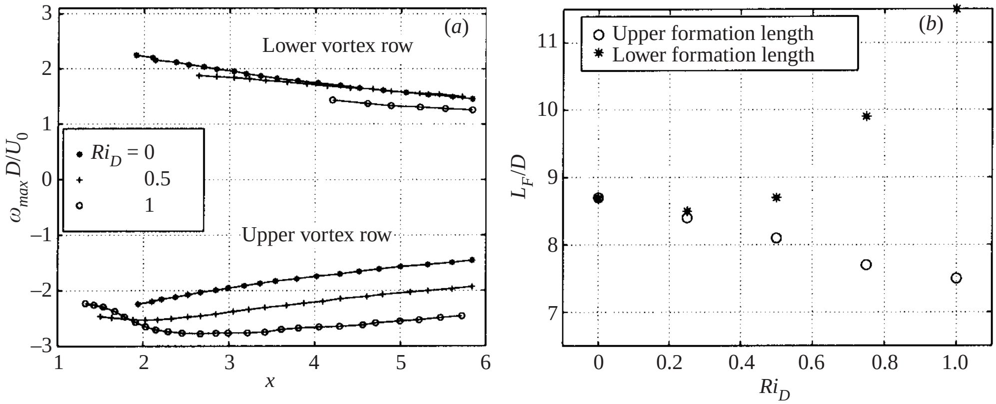

FIGURE 17. Effect of Ri_D on (a) the the local vorticity absolute peak values and (b) the formation length L_F for $Re_D = 75$.

Illustrative is the effect of heat on the formation length L_F of the vortices, where the formation length L_F is defined as the x-distance between the cylinder centre and the centre of a vortex structure just after its formation. A just-formed vortex is defined here as the area with a local vorticity extreme ω_{max} bounded by a closed vorticity contour $0.1\omega_{max}$. By increasing Ri_D the formation length of the upper vortex decreases (figure 17b). Apparently, the net negative production promotes the formation of an upper vortex. On the other hand, the net negative production seems to retard the formation of the lower vortex for $Ri_D > 0.25$, thus increasing its formation length.

7. Conclusion

The results show that due to the heat added by the cylinder, the vortices in the upper and lower vortex row acquire different strengths (in an absolute sense). This strength difference increases for increasing Ri_D and is already present just after the vortex structures are shed. As a result, the shed vortices are seen to move slightly downwards. At first sight, this is a rather unexpected behaviour, considering the upward action of the buoyancy force. By using a point-vortex model it is shown that the strength difference is indeed responsible for the observed negative deflection. The point-vortex model predicts a continuously increasing downward shift of the vortices. This is in contrast to the experimental and numerical results, which show a maximum downward deflection for $Ri_D = 0.5$. For higher values of Ri_D the thermally induced buoyancy force causes the vortex structures to move up again, compensating the effect of the strength difference. A second effect of the strength difference is the relative motion between the vortex structures, visible as a rotational drift of the lower vortex around its upper neighbour.

It has been shown that various heat-induced effects play a role during the vortex formation process. Together, these effects are responsible for the observed difference in structure characteristics such as temperature and strength of the upper and lower vortices. To address all the effects, one needs to separate the effects of heat on the flow behaviour in the region close to the cylinder ($-1 < x < 1$) from those in the formation region ($1 < x < 6$–8). In the present study the narrow region around the cylinder $-1 < x < 1$ is considered as a vorticity source from which vorticity is advected into the downstream region $x > 1$. The results show that for $Ri_D > 0$, slightly more positive than negative vorticity is produced and transported into the region $x > 1$ (figure 14).

This is in contrast with the results found for the fully developed structures at $x > 8$, where the negative upper vortex structures are stronger than the lower ones (with positive vorticity).

The second (and most important) process is the baroclinic vorticity production in the region $1 < x < 4$. In this region, the vorticity production is mostly negative. Also, the areas where vorticity is produced coincide with the region where a vortex structure is growing. This means that vorticity production in the region considered adds to the negative vorticity structures and causes the positive vorticity structures to become weaker. This effect can be observed in the plot of peak vorticity of the structures as a function of their downstream position for $Ri_D > 0$ (figure 17).

In conclusion, it may be stated that the strength difference between the upper and lower vortices, observed in the case when heat is added to the cylinder, is caused by thermally induced baroclinic-vorticity production in the near-wake region. This process is different for the upper and lower vortex structures, leading to an asymmetry in the wake. The strength difference in turn is responsible for the remarkable downward deflection of the entire vortex street and the relative drift of the wake vortex structures. It is interesting to investigate whether this also holds for other values of the Reynolds and Prandtl numbers.

This work is part of the research programme of the Netherlands Foundation for Fundamental Research on Matter (FOM), which is financially supported by the Netherlands Organisation for Scientific Research (NWO). The authors would like to take the opportunity to thank the technical staff of the Section Energy Technology of the Department of Mechanical Engineering for their support.

REFERENCES

Agui, C. & Jimenez, J. 1987 On the performance of particle tracking. *J. Fluid Mech.* **185**, 447–468.

Badr, H. 1984 Laminar combined convection from a horizontal cylinder-parallel and contra flow regimes. *Intl J. Heat Mass Transfer* **27**, 15–27.

Bastiaans, R., van der Plas, G. & Kieft, R. 2001 The performance of a new PTV algorithm applied in super-resolution PIV. *Exps. Fluids* **32**, 346–356.

Davies, M. 1976 A comparison of the wake structure of a stationary and oscillating bluff body, using a conditional averaging technique. *J. Fluid Mech.* **75**, 209–231.

Dennis, S., Nguyen, P. & Kocabiyik, S. 2000 The flow induced by a rotationally oscillating and translating circular cylinder. *J. Fluid Mech.* **407**, 123–144.

Green, R. & Gerrard, J. 1991 An optical interferometric study of the wake of a bluff body. *J. Fluid Mech.* **226**, 219–242.

Griffin, O. & Ramberg, E. 1976 Vortex shedding from a cylinder vibrating in line with an incident uniform flow. *J. Fluid Mech.* **75**, 257–271.

Griffin, O. & Votaw, C. 1971 The vortex street in the wake of a vibrating cylinder. *J. Fluid Mech.* **55**, 31–48.

Karasudani, T. & Funakoshi, M. 1994 Evolution of a vortex street in the far wake of a cylinder. *Fluid Dyn. Res.* **14**, 331–352.

Karniadakis, E. & Triantafyllou, G. 1989 Frequency selection and asymptotic states in laminar wakes. *J. Fluid Mech.* **199**, 441–469.

Kieft, R. 2000 Mixed convection behind a heated cylinder. PhD thesis, Eindhoven University of Technology, The Netherlands.

Kieft, R., Rindt, C. & van Steenhoven, A. 1999 The wake behaviour behind a heated horizontal cylinder. *Expl Therm. Fluid Sci.* **19**, 183–193.

Koopmann, G. 1967 The vortex wakes of vibrating cylinders at low Reynolds numbers. *J. Fluid Mech.* **28**, 501–512.

Maday, Y., Patera, A. & Ronquist, E. 1990 An operator-integration-factor splitting method for time-dependent problems: Applications to compressible flow. *J. Sci. Comput.* **5**, 263–291.

Michaux-Leblond, N. & Bélorgey, M. 1997 Near-wake behavior of a heated circular cylinder: viscosity-buoyancy duality. *Expl Therm. Fluid Sci.* **15**, 91–100.

Minev, P., van de Vosse, F., Timmermans, L. & van Steenhoven, A. 1996 A second order splitting algorithm for thermally-driven flow problems. *Intl J. Numer Meth. Heat Fluid Flow* **6**, 51–60.

Noto, K. 1990 Computational investigation on wake behavior with buoyancy from a heated elliptic cylinder: Effect of mainstream attack angle. In *Thirty-ninth Japanese National Congress of Applied Mechanics*, pp. 293–303. University of Tokyo Press.

Noto, K., Ishidea, H. & Matsumoto, R. 1983 A break-down of the von Kármán vortex street due to the natural convection. In *Flow Visualization 3* (ed. W.-J. Yang), pp. 348–354. Springer.

Noto, K. & Matsumoto, R. 1987 Numerical simulation on the development of the Karman vortex street due to the negatively buoyant force. In *Fifth Conf. on Numerical Methods in Laminar and Turbulent Flow* (ed. C. Taylor, W. G. Habashi & M. M. Hafez), pp. 796–809. Pineridge Press, Swansea.

Timmermans, L., Minev, P. & van de Vosse, F. 1996 An approximate projection scheme for incompressible flow using spectral elements. *Intl J. Numer Meth. Fluids* **22**, 673–688.

van de Vosse, F., Minev, P. & Timmermans, L. 1995 A spectral element projection scheme for incompressible flow with application to shear-layer stability studies. In *Third Intl Conf. on Spectral and High Order Methods*, pp. 295–304. Houston Journal of Mathematics, University of Houston.

Williamson, C. 1989 Oblique and parallel modes of vortex shedding in the wake of a circular cylinder at low Reynolds numbers. *J. Fluid Mech.* **206**, 579–627.